PCCP

PAPER

View Article Online
View Journal | View Issue

Cite this: *Phys. Chem. Chem. Phys.*, 2023, **25**, 2212

Structure and magnetism of electrospun porous high-entropy $(Cr_{1/5}Mn_{1/5}Fe_{1/5}Co_{1/5}Ni_{1/5})_3O_4$, $(Cr_{1/5}Mn_{1/5}Fe_{1/5}Co_{1/5}Zn_{1/5})_3O_4$ and $(Cr_{1/5}Mn_{1/5}Fe_{1/5}Ni_{1/5}Zn_{1/5})_3O_4$ spinel oxide nanofibers†

Alessandro Ponti, *[a] Claudia Triolo, [bc] Beatrix Petrovičovà, [b] Anna M. Ferretti, [a] Gioele Pagot, [d] Wenlei Xu, [e] Vito Di Noto, [d] Nicola Pinna *[e] and Saveria Santangelo *[bc]

Received 2nd November 2022,
Accepted 14th December 2022

DOI: 10.1039/d2cp05142g

rsc.li/pccp

High-entropy oxide nanofibers, based on equimolar (Cr,Mn,Fe,Co,Ni), (Cr,Mn,Fe,Co,Zn) and (Cr,Mn,Fe,Ni,Zn) combinations, were prepared by electrospinning followed by calcination. The obtained hollow nanofibers exhibited a porous structure consisting of interconnected nearly strain-free $(Cr_{1/5}Mn_{1/5}Fe_{1/5}Co_{1/5}Ni_{1/5})_3O_4$, $(Cr_{1/5}Mn_{1/5}Fe_{1/5}Co_{1/5}Zn_{1/5})_3O_4$ and $(Cr_{1/5}Mn_{1/5}Fe_{1/5}Ni_{1/5}Zn_{1/5})_3O_4$ single crystals with a pure $Fd\bar{3}m$ spinel structure. Oxidation state of the cations at the nanofiber surface was assessed by X-ray photoelectron spectroscopy and cation distributions were proposed satisfying electroneutrality and optimizing octahedral stabilization. The magnetic data are consistent with a distribution of cations that satisfies the energetic preferences for octahedral *vs.* tetrahedral sites and is random only within the octahedral and tetrahedral sublattices. The nanofibers are ferrimagnets with relatively low critical temperature more similar to cubic chromites and manganites than to ferrites. Replacing the magnetic cations Co or Ni with non-magnetic Zn lowers the critical temperature from 374 K (Cr,Mn,Fe,Co,Ni) to 233 and 105 K for (Cr,Mn,Fe,Ni,Zn) and (Cr,Mn,Fe,Co,Zn), respectively. The latter nanofibers additionally have a low temperature transition to a reentrant spin-glass-like state.

Introduction

High-entropy materials (HEMs) are a new class of materials consisting in multicomponent solid solutions. Multicomponents, present in near-equimolar proportions, are randomly distributed in the lattice.[1,2] They are attracting enormous scientific attention due to their unique structure, enhanced properties, novel functionalities and potential for application in many different fields ranging from catalysis to energy storage and conversion.[3–20]

The class of HEMs encompasses materials having bonding character spanning from metallic to ionic and a variety of structures (hexagonal, cubic, rock-salt, fluorite, perovskite, spinel...), featured by high-entropy mixing at one or two cation sublattice(s).[21] HEMs comprise high-entropy alloys (HEAs)[1,2] and high-entropy ceramics (HECs),[21,22] in turn including sulfides,[23] silicides,[24] nitrides,[25] carbides,[26] oxides[10,27–29] and other compounds.[30]

After the synthesis of the first single-phase multicomponent rock-salt oxide *via* solid state sintering from an equimolar mixture of binary oxides in 2015,[28,31] many physical or chemical routes have been followed in the last years to prepare HEMs in various forms (bulk, nanoparticles, nanosheets...).[22,32–38] Very recently, it has been demonstrated that high entropy oxides (HEOs) in the form of nanofibers (NFs) can be successfully prepared by the electrospinning technique.[39–43] Zhao *et al.*[39] have reported the synthesis of electrospun high entropy $(La_{1/5}Sm_{1/5}Eu_{1/5}Gd_{1/5}Tm_{1/5})_2Zr_2O_7$ NFs with excellent thermal

[a] *Laboratorio di Nanotecnologie, Istituto di Scienze e Tecnologie Chimiche "Giulio Natta" (SCITEC), Consiglio Nazionale delle Ricerche, Via Fantoli 16/15, 20138 Milano, Italy. E-mail: alessandro.ponti@scitec.cnr.it*
[b] *Dipartimento di Ingegneria Civile, dell'Energia, dell'Ambiente e dei Materiali (DICEAM), Università "Mediterranea", Loc. Feo di Vito, 89122 Reggio Calabria, Italy. E-mail: saveria.santangelo@unirc.it*
[c] *National Reference Center for Electrochemical Energy Storage (GISEL), Consorzio Interuniversitario Nazionale per la Scienza e Tecnologia dei Materiali (INSTM), 50121 Firenze, Italy*
[d] *Section of Chemistry for the Technology (ChemTech), Department of Industrial Engineering, University of Padova, Via Marzolo 9, 35131 Padova, PD, Italy*
[e] *Institut für Chemie and IRIS Adlershof, Humboldt-Universität zu Berlin, Brook-Taylor Str. 2, 12489 Berlin, Germany. E-mail: nicola.pinna@hu-berlin.de*

† Electronic supplementary information (ESI) available. See DOI: https://doi.org/10.1039/d2cp05142g

stability, whereas Xing *et al.*[40] have produced $(Y_{1/5}Yb_{1/5}Sm_{1/5}Eu_{1/5}Er_{1/5})_2O_3$ NFs with cubic bixbyite structure.

High entropy rock-salt $(Mg_{1/5}Co_{1/5}Ni_{1/5}Cu_{1/5}Zn_{1/5})O$ NFs prepared *via* electrospinning have shown interesting performance as active anode materials in rechargeable lithium ion batteries.[41,42] Electrospinning is a simple, versatile and cost-effective technique, widely adopted for the production of porous high aspect ratio nanostructures and suitable for the manufacturing of NFs on an industrial scale due to its scalability.[44–48] This paper deals with the preparation and thorough characterization of electrospun porous NFs of high-entropy (Cr,Mn,Fe,Co,Ni), (Cr,Mn,Fe,Co,Zn) and (Cr,Mn,Fe,Ni,Zn) oxides having spinel structure. This structure comprises a slightly distorted face-centered cubic (fcc) lattice of O^{2-} anions, where cations occupy tetrahedral 8a sites and octahedral 16d sites, thus forming two cation sublattices (Fig. S1, ESI†).[49] High entropy spinel oxides (HESOs) have been the focus of in-depth studies.[50–57]

Among them, $(Cr_{1/5}Mn_{1/5}Fe_{1/5}Co_{1/5}Ni_{1/5})_3O_4$, the first HESO to be reported,[50] has received particular attention and has been evaluated for several applications, such as electrocatalysis[53,54] and energy storage.[52,55,58] The magnetic properties of HESOs have already been summarized.[59,60] They are governed by the oxido-mediated superexchange interactions within and between the two cation sublattices. The magnetic properties of $(Cr_{1/5}Mn_{1/5}Fe_{1/5}Co_{1/5}Ni_{1/5})_3O_4$, in both bulk and nanostructured form,[61–65] have been the subject of several studies, which have firmly established that $(Cr_{1/5}Mn_{1/5}Fe_{1/5}Co_{1/5}Ni_{1/5})_3O_4$ is a ferrimagnet below *ca.* 400 K. The low temperature behavior has been attributed to antiferromagnetically-coupled regions rich in Cr or Mn[62] or locally varying inter-site exchange interactions.[65] Mao *et al.*[61] have reported the magnetization isotherms at room temperature (RT) of $(Cr_{1/5}Mn_{1/5}Fe_{1/5}Co_{1/5}Zn_{1/5})_3O_4$ and $(Cr_{1/5}Mn_{1/5}Fe_{1/5}Ni_{1/5}Zn_{1/5})_3O_4$ and shown that substitution of nonmagnetic Zn^{2+} for magnetic Co^{2+} and Ni^{2+} decreases the saturation and remanent magnetization, and coercive field.

Here, a detailed magnetic characterization of electrospun $(Cr_{1/5}Mn_{1/5}Fe_{1/5}Co_{1/5}Ni_{1/5})_3O_4$, $(Cr_{1/5}Mn_{1/5}Fe_{1/5}Co_{1/5}Zn_{1/5})_3O_4$ and $(Cr_{1/5}Mn_{1/5}Fe_{1/5}Ni_{1/5}Zn_{1/5})_3O_4$ NFs is presented. These HESO-NFs display a rich and diverse magnetic behavior depending on composition. The present study confirms that $(Cr_{1/5}Mn_{1/5}Fe_{1/5}Co_{1/5}Ni_{1/5})_3O_4$ NFs have ferrimagnetic structure between 5 and $\approx$400 K but, at variance with previous interpretation, the structure is non-collinear, *i.e.*, the sublattice magnetizations are not parallel. We prove that both $(Cr_{1/5}Mn_{1/5}Fe_{1/5}Co_{1/5}Zn_{1/5})_3O_4$ and $(Cr_{1/5}Mn_{1/5}Fe_{1/5}Ni_{1/5}Zn_{1/5})_3O_4$ NFs are paramagnetic at RT and upon cooling they first assume a non-collinear ferrimagnetic structure and then a conical/spiral or canted ferrimagnetic structure with spin-glass-like character. The qualitative similarity of the Zn-containing NFs is, however, contrasted by the largely different magnetic parameters and transition temperatures. Therefore, the magnetic structure of HESO-NFs can be easily tuned by changing just a single cation. This study paves the way to the obtainment of one-dimensional nanostructures with controlled and easily tailored magnetic properties, which is of great applicative interest as they can potentially be used as building blocks for next-generation electromagnetic devices,[66] in magnetic sensors, and flexible magnets.[67]

Results and discussion

Morphology of the HESO-NFs

Based on the varying cations in the transition metal (TM) combinations, the produced (Cr,Mn,Fe,Co,Ni), (Cr,Mn,Fe,Co,Zn) and (Cr,Mn,Fe,Ni,Zn) HESOs were coded as CoNi, CoZn and NiZn (Fig. S2e, ESI†).

Fig. S3 (ESI†) displays the results of the scanning electron microscopy/energy-dispersive X-ray spectroscopy (SEM/EDX) analysis on the as-calcined samples. SEM micrographs demonstrate the formation of NFs for all compositions. Nonetheless, slight changes are noticed in their morphology (Fig. S3a–c, ESI†). In sample CoNi (Fig. S3a, ESI†), where bundles of NFs alongside isolated NFs are observed, the fibers look relatively uniform in diameter along their axis. On the contrary, in samples CoZn (Fig. S3b, ESI†) and NiZn (Fig. S3c, ESI†), the diameter is not uniform along the NF axis; the variation is more marked in the case of the latter sample. The center of the NF diameter distributions (Fig. S3d–f, ESI†), as measured by the image analysis software of the microscope, decreases in the order CoNi > CoZn > NiZn. EDX analysis (Fig. S3g–i, ESI†) proves the spatially uniform distribution of oxygen and TMs throughout all samples at the micro-scale.

Fig. 1 and Fig. S4–S6 (ESI†) summarize the results of high-resolution transmission electron microscopy/scanning transmission electron microscopy (HRTEM/STEM)/EDX analysis. The TEM images with lower magnification (Fig. S4a, c and e, ESI†) substantially confirm the morphological picture emerged from the SEM analysis. Apart from the above-described slight differences, the morphology of the NFs exhibits common features to all the compositions. The fibers, with diameters in the 150–450 nm range, are micrometer long and featured by a coral-like structure (Fig. 1a–c), as frequently observed in electrospun oxides.[68–70] They consist of interconnected grains with size ranging between a few tens of nm to the hundred nm range.

Regardless of their composition, the primary oxide grains have well defined polyhedral shape, with more or less rounded vertices (Fig. 1d–h and Fig. S5, ESI†). The oxide grains are crystalline with spinel structure and randomly oriented, as proved by the diffraction rings in the selected-area electron diffraction (SAED) patterns (Fig. 1i and Fig. S6a, d, ESI†) for isolated NFs (Fig. 1j and Fig. S6b, e, ESI†). They exhibit a spinel structure. The STEM/EDX elemental maps (Fig. 1k and Fig. S6c, f, ESI†) reveal that in all samples the spatial distribution of metals and oxygen is homogeneous even at the nanometer scale.

The compositional analysis by STEM/EDX highlights the achievement of nearly equiatomic combinations of TMs (Fig. 1l–n), namely $(Cr_{0.18}Mn_{0.21}Fe_{0.18}Co_{0.22}Ni_{0.21})$, $(Cr_{0.19}Mn_{0.22}Fe_{0.18}Co_{0.22}Zn_{0.19})$ and $(Cr_{0.20}Mn_{0.16}Fe_{0.19}Ni_{0.22}Zn_{0.23})$ for samples CoNi, CoZn and NiZn, respectively.

The homogeneity of the cation distribution is further confirmed by the projection analysis of the EDX maps (Fig. 2). The

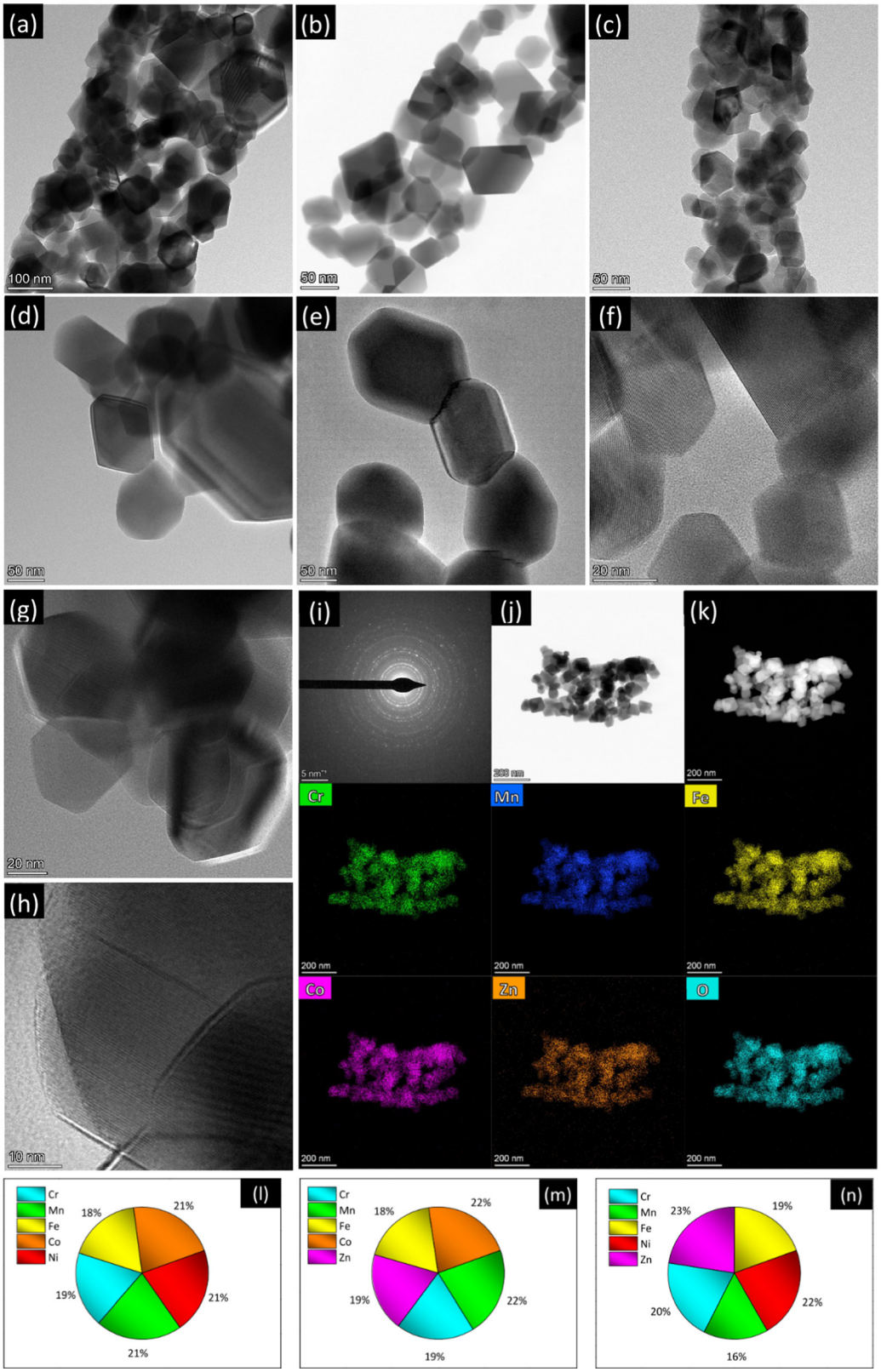

Fig. 1 Results of the HRTEM/STEM/EDX analysis on samples (a, d, g, h and l) CoNi, (b, e, i–k and m) CoZn and (c, f and n) NiZn. (a–h) HRTEM images; (i) SAED pattern for (j) an isolated NF, (k) corresponding STEM/EDX elemental maps and (l–n) relative concentrations of the TMs.

normalized profiles of all the metals and oxygen overlap to within the experimental noise, except for a small discrepancy of the Zn profile in the CoZn NF (Fig. 2b). Model profiles for solid or hollow NFs were fitted to the experimental oxygen profiles of

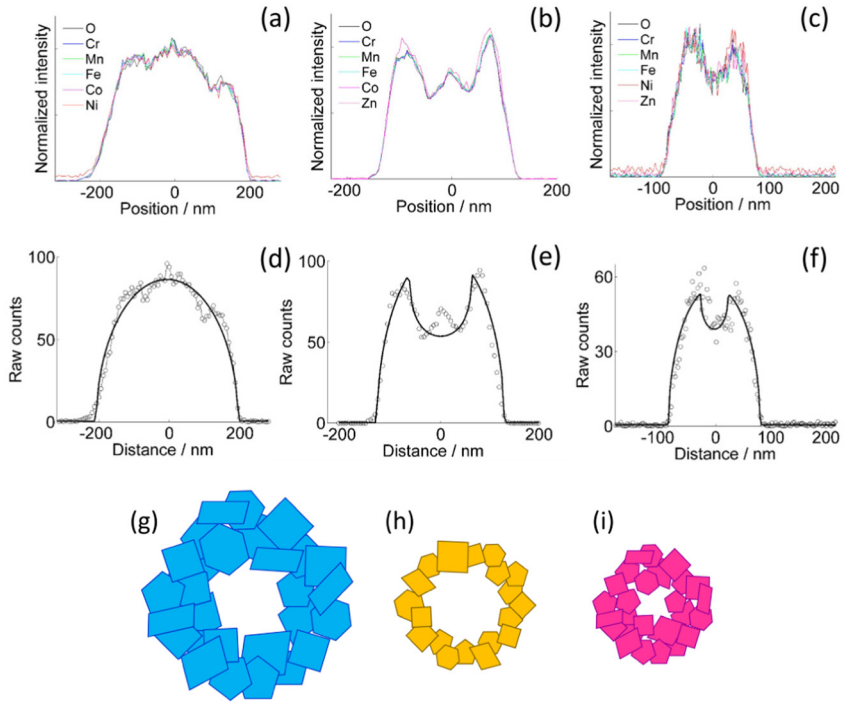

Fig. 2 Projection analysis of the EDX elemental maps. (a–c) Projected profiles of a quasi-solid NF (a, CoNi), irregularly hollow NF (b, CoZn), and hollow NF (c, NiZn). (d–f) Experimental oxygen profiles (circles) and best-fit models (line). (g–i) Sketch of the typical cross section of (g) CoNi, (h) CoZn and (i) NiZn NFs. Note the different length scales in panels (a–f).

selected NFs (Fig. 2d–f). Comparing results for each NF, the NFs were assigned to three morphological categories, namely, quasi-solid, irregularly hollow, and hollow NF. All morphologies were observed for each NF composition and irregularly hollow NFs seem predominant in all samples. In addition to categorizing the NP morphology, the fitting procedure allowed measuring the NF outer and inner diameter of the selected NFs. The range of both diameters are collected in Table S2 (ESI†) along with that of the calculated shell thickness, and cross-section sketches of the three NF types are shown in Fig. 2g–i.

The decreasing trend of the outer NF diameter CoNi > CoZn > NiZn resulting from projection analysis agrees with the NP diameter distribution from the analysis of SEM images. Electron diffraction patterns proved that the NF comprise primary particles with spinel structure. HRTEM images of samples CoNi, CoZn and NiZn display crystal lattice fringes in primary particles that are suitably oriented with respect to the electron beam. Geometrical phase analysis (GPA) of the crystal lattice fringes allowed monitoring the crystallinity of the primary particles and the crystallographic relationship with neighboring particles (Fig. 3). Fringes were observed for the {111}, {220}, and {311} planes. No difference among the three NF samples was found, so the following discussion applies to all NF types. All fringe-displaying particles are single crystals and are free from significant strain, except for thin strained layers where the particles are in contact (Fig. 3g).

A single case in a CoNi NF was observed, where a 40 × 60 nm polyhedral, round-edged particle displays compressive strain along its free edges (Fig. 3g). It is interesting that in all cases no significant strain is observed in the particle interior. In general, equal orientation of neighboring particles is not observed by HRTEM, even when they are face-sharing. Only in a few cases, equi-oriented particles are detected (Fig. 3b, e and h). In conclusion, GPA of HRTEM fringes showed that (i) the characteristics of the primary particles are common to the three NF samples, (ii) the primary particles are single crystals, and (iii) neighboring particles usually have different lattice orientation, the opposite is rarely detected in HRTEM images.

Crystalline phase of the oxide

Fig. 4 shows the XRD patterns of the electrospun HESO-NFs. In all samples, the diffraction peaks correspond to the reflections of fcc spinel structure, belonging to $Fd\bar{3}m$ space group (JCPDS no. 22-1084)[51,52,56,61,71–76] No additional peaks attributable to secondary phases are detected, indicating that a single-phase is formed for any composition, namely $(Cr_{1/5}Mn_{1/5}Fe_{1/5}Co_{1/5}Ni_{1/5})_3O_4$, $(Cr_{1/5}Mn_{1/5}Fe_{1/5}Co_{1/5}Zn_{1/5})_3O_4$ $(Cr_{1/5}Mn_{1/5}Fe_{1/5}Co_{1/5}Ni_{1/5})_3O_4$, $(Cr_{1/5}Mn_{1/5}Fe_{1/5}Co_{1/5}Zn_{1/5})_3O_4$ and $(Cr_{1/5}Mn_{1/5}Fe_{1/5}Ni_{1/5}Zn_{1/5})_3O_4$ for samples CoNi, CoZn and NiZn, respectively. This finding is in agreement with the outcomes provided by the SAED patterns. The average size of HESO crystallites (*i.e.*, coherence length) is calculated from the full width at half maximum (FWHM) of the (331) peak, through the Scherrer's equation, $d = k\lambda/\beta\cos\theta$, where k (0.9) is the shape factor, λ is the wavelength of X-ray radiation, β is the FWHM in radians and θ is the Bragg's angle.[77]

The obtained values increase in the order CoZn (83.7 nm) < CoNi (97.0 nm) < NiZn (98.5 nm), respectively.

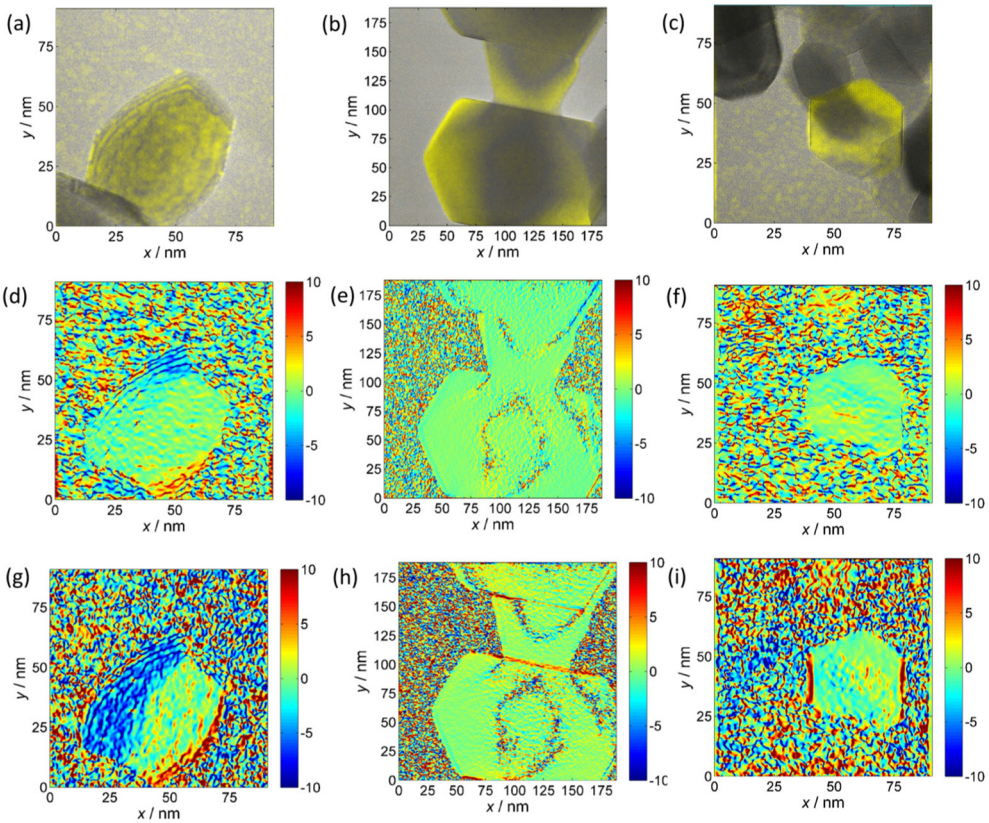

Fig. 3 Geometrical phase analysis of the NFs. (a–c) Intensity-colorized maps, (d–f) lattice rotation maps (°), and (g–i) lattice strain maps (% cell size). All primary particles are single crystals. The particle in panels (c, f and i) has no crystallographic relationship with its numerous neighbors whereas the particles in panels (b, e and h) are equi-oriented. The particle in panels (a, d and g) displays significant strain along its long edges that are not in contact with other particles. The shown data refer to NFs (a, d and g) CoNi, (b, e and h) CoZn and (c, f and i) NiZn.

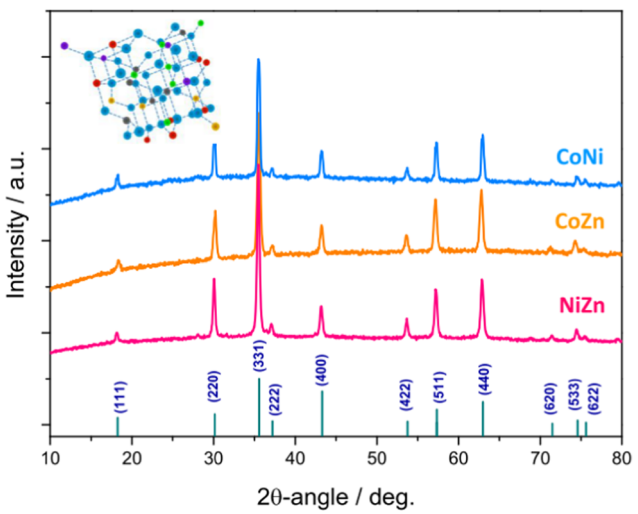

Fig. 4 XRD patterns of the HESO-NFs.

The lattice constants, as inferred from Rietveld analysis (Fig. S7, ESI†), increase in the order CoNi (8.3215(8) Å) < NiZn (8.3256(6) Å) < CoZn (8.3712(8) Å). The variation is in the same order as the average ionic radius of divalent cations (Co^{2+}, Ni^{2+} in sample CoNi, Co^{2+}, Zn^{2+} in sample CoZn, and Ni^{2+}, Zn^{2+} in sample NiZn).[78,79]

Surface composition of HESO-NFs and oxidation states of cations

Fig. S8 (ESI†) shows the X-ray photoelectron spectroscopy (XPS) survey spectra of the investigated HESO-NFs. The high-resolution X-ray photoelectron (HR-XPS) spectra of the core levels are displayed in Fig. 5. The resulting surface composition is reported in Table S3 (ESI†). In all samples, the analysis reveals that Cr, Mn, Fe and O, as well as adventitious carbon, are present on the surface. Ni and Co, Co and Zn, Ni and Zn are also detected in samples CoNi, CoZn and NiZn, respectively.

The HR-XPS spectra of Cr2p core level (Fig. 5a, g and m) are featured by two couples of spin–orbit components centered at binding energies (BEs) of *ca.* 576.0 and 578.3 eV ($2p_{3/2}$) and 585.6 and 587.8 eV ($2p_{1/2}$) in all samples. This indicates the presence of two different Cr-based species on the surface of the investigated materials: (i) the dominant component (see Table S4, ESI†), with its two spin–orbit features at the lower BE values, is attributed to Cr(III) species present into mixed TM spinel oxides, in accordance with the literature;[80,81] and (ii) the second component points to the possible presence of chromium in its high oxidation state (*i.e.*, VI).[82] The co-presence of Cr^{6+} surface

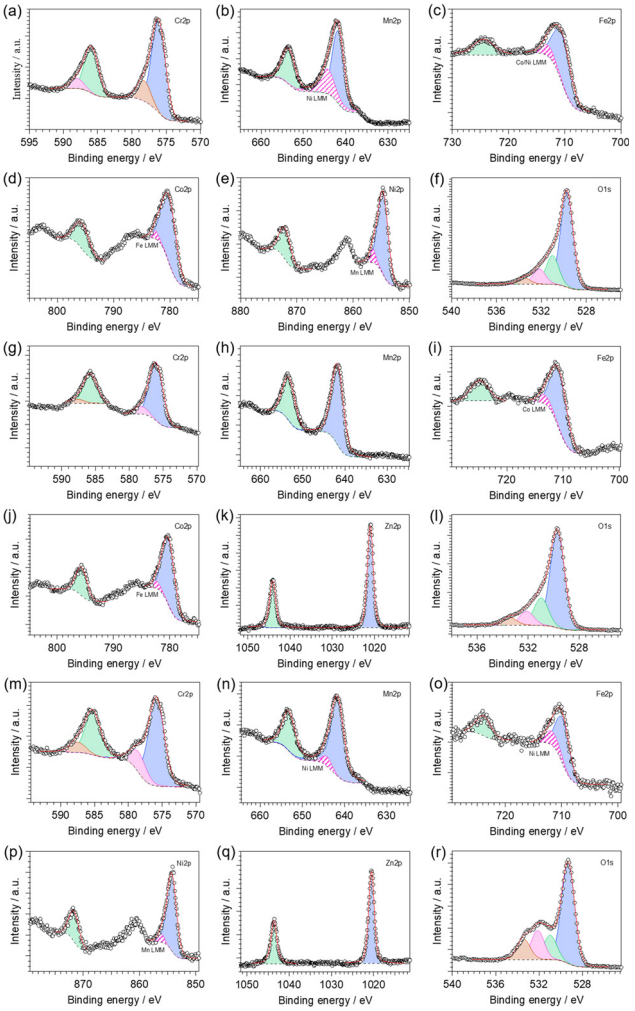

Fig. 5 High-resolution XPS spectra for samples (a–f) CoNi, (g–l) CoZn and (m–r) NiZn and deconvolution in the different spectral regions: Cr2p (a, g and m); Mn2p (b, h and n); Fe2p (c, i and o); Co2p (d and j); Ni2p (e and p); Zn2p (k and q); and O1s (f, l and r).

species has been reported also for $(Cr_{1/5}Mn_{1/5}Fe_{1/5}Co_{1/5}Ni_{1/5})_3O_4$ HEO nanoparticles synthesized *via* a surfactant-assisted hydrothermal method.[74] It has been attributed to the oxidation of the sample surface, taking place during the 900 °C heat treatment in air.

In the Mn2p region (Fig. 5b, h and n), HR-XPS spectra reveal the presence of one type of manganese species with the characteristic two peaks as result of the spin–orbit splitting. The $Mn2p_{3/2}$ component is peaking at *ca.* 641.8 eV, which is closer to the BE value typical of Mn(III) rather than other oxidation states, as observed in similar materials.[80] In samples CoNi and NiZn, the $Mn2p_{3/2}$ peak overlaps with a Ni LMM Auger line (Fig. S8, ESI†).[83]

The HR-XPS spectra of Fe2p core level (Fig. 5c, i and o) two peaks are detected located at BEs of *ca.* 710 and 724 eV (for the $2p_{3/2}$ and $2p_{1/2}$ features, respectively). Interestingly, the BE values of $Fe2p_{3/2}$ peaks decrease in the order CoZn (710.8 eV) > CoNi (710.4 eV) > NiZn (709.8 eV); the BEs of $Fe2p_{1/2}$ peaks behave analogously. All these values are comprised between the BEs of Fe(III) in Fe_2O_3 and that of Fe(II) in FeO, which are typically observed at *ca.* 711.2 and 709.5 eV, respectively.[80] Thus, on the surface of all investigated HESO-NFs, iron is expected to be found as a mixture of both III and II oxidation states, with the former mostly present in sample CoZn, and the latter in the sample NiZn. The co-presence of Fe^{3+} and Fe^{2+} species in spinel HEOs has been reported also by other authors.[74]

In CoNi, CoZn and NiZn samples, the $Fe2p_{3/2}$ peak overlaps with a Ni LMM and/or Co LMM Auger lines (Fig. S8, ESI†).[83]

In samples CoNi and CoZn, the HR-XPS spectra of Co2p core level (Fig. 5d and j, respectively) are featured by two spin–orbit components centered at BEs of *ca.* 780.2 eV ($2p_{3/2}$) and 795.6 eV ($2p_{1/2}$). Typically, Co(II) and Co(III) are difficult to be distinguished, due to a similar BE value at *ca.* 780.6 eV.[80,83] Nevertheless, the appearance of strong satellite peaks, as observed in the investigated materials, indicates that cobalt atoms are present mainly as Co(II).[80,84,85] The $Co2p_{3/2}$ peak overlaps with a Fe LMM Auger line (Fig. S8, ESI†).[83]

In the Ni2p region, HR-XPS spectra of samples CoNi and NiZn (Fig. 5e and p, respectively) reveal the presence of one type of nickel species with the characteristic two peaks as result of the spin–orbit splitting. The $Ni2p_{3/2}$ component is peaking at *ca.* 854.5 eV, which is similar to the BE value typical of Ni(II) in NiO and in mixed oxides of nickel and other metals.[80] In addition, the presence of satellite peaks corroborates the hypothesis that nickel atoms are present in the Ni(II) oxidation state.[80,84,85] The $Ni2p_{3/2}$ peak overlaps with a Mn LMM Auger line (Fig. S8, ESI†).[83]

In the Zn2p region of HR-XPS spectra of samples CoZn and NiZn (Fig. 5k and q, respectively), two strong peaks centered at *ca.* 1020.8 and 1043.9 eV appear. They are assigned to the $Zn2p_{3/2}$ and $Zn2p_{1/2}$ spin–orbit components, respectively. The observed BEs are characteristic of ZnO,[86,87] indicating that: (i) zinc is present as Zn(II); and (ii) apparently, zinc hydroxide is not present on the surface of these samples.

Finally, for all analyzed samples, a strong peak is observed in the O1s region (Fig. 5f, l and r). It can be decomposed in three different features (the relative amounts are reported in Table S4, ESI†). In the HR-XPS spectra of O1s core level, (i) the dominant contribution, centered at *ca.* 529.5 eV, is assigned to lattice O^{2-} ions (OL) belonging to mixed TM oxides;[88–91] (ii) the peak present at *ca.* 531.0 eV is attributed to native defects of O_2-vacancies (OV);[88–91] and (iii) the peaks centered at high BEs (*i.e.*, at *ca.* 532.1 and 533.4 eV) are associated with adsorbed or chemisorbed oxygen species, such as O_2 or H_2O.[92–94] The fraction of OV increases in the order CoNi > NiZn ≈ CoZn (see Table S4 in ESI†), indicating that the chemical composition of the HEM can control the concentration of oxygen vacancies into the material.

Phase purity of the oxide and inversion degree of the spinel phase

In order to get a deeper insight into the phase purity and crystallinity of the produced HESO-NFs, micro-Raman analysis was carried out. Spectra from several random positions on each

specimen were recorded and compared to each other to evaluate the spatial homogeneity of the samples in terms of crystalline phase (Fig. S9, ESI†). The lack of significant differences in the relative intensities and shifts in the positions of the bands confirms the formation of a single oxide phase in each sample, without appreciable local deviations from the average chemical composition.[71]

Fig. 6 displays the averaged spectra with the apparent peak positions. According to the factor group analysis, the predicted normal vibration modes of the $Fd\bar{3}m$ spinels ($A_{1g} + E_g + F_{1g} + 3F_{2g} + 2A_{2u} + 2E_u + 4F_{1u} + 2F_{2u}$) include 39 optical modes and 3 acoustic modes.[49,95–99] The triply degenerate F_{1u} modes are infrared-active, whereas the A_{1g}, doubly degenerate E_g and triply degenerate F_{2g} modes are Raman-active.[49,95,97,99] The remaining modes are inactive.[49,96] All Raman-active modes involve the motions of oxygen along the cubic space diagonals.[100,101] The A_{1g} mode is due to the vibration along the direction joining an oxygen atom to the tetrahedral M^{2+} cation and usually appears between 600 and 720 cm^{-1}.[95,99,102–105] The E_g mode, detected between 250 and 360 cm^{-1},[103–105] is associated to symmetric bending of O^{2-} anion with respect to octahedral M^{3+} cation.[103] The $F_{2g}(1)$ mode, appearing between 160 and 220 cm^{-1},[103–105] originates from translation motion of M^{3+}–O^{2-}, while higher frequency $F_{2g}(2)$ and $F_{2g}(3)$ modes, between 440 and 590 cm^{-1},[95,102–104] arise from the asymmetric stretching and asymmetric bending of oxygen, respectively.[104]

Both positions of the Raman bands and their relative intensities strongly vary within the family of spinels.[95,98,104–108] Just to cite some cases, the most intense A_{1g} mode is detected at 630 cm^{-1} in $ZnFe_2O_4$ and 690 cm^{-1} in $NiFe_2O_4$;[104] the E_g mode, located at 320 cm^{-1} in $NiFe_2O_4$, downshifts at 250 cm^{-1} in $ZnFe_2O_4$,[104] whereas the $F_{2g}(1)$, $F_{2g}(2)$ and $F_{2g}(3)$ modes appear respectively at 180, 470 and 570 cm^{-1} in $NiFe_2O_4$ and at 160, 350 and 450 cm^{-1} in $ZnFe_2O_4$.[104] In $CoFe_2O_4$, the $F_{2g}(1)$, E_g, $F_{2g}(2)$, $F_{2g}(3)$ and A_{1g} modes are located at 162, 302, 463, 613 and 678 cm^{-1}, respectively.[105] In magnetite ($FeFe_2O_4$), the $F_{2g}(1)$ is not detected, while the E_g, $F_{2g}(2)$, $F_{2g}(3)$ and A_{1g} modes appear at 312, 474, 548 and 677 cm^{-1}, respectively.[95]

The same occurs in $FeCr_2O_4$, where the E_g, $F_{2g}(2)$, $F_{2g}(3)$ and A_{1g} modes are detected at 436, 493, 591 and 674 cm^{-1}, respectively.[95] In $ZnCr_2O_4$, the $F_{2g}(1)$, E_g, $F_{2g}(2)$, $F_{2g}(3)$ and A_{1g} modes appear at 182, 452, 511, 605 and 688 cm^{-1}, respectively,[95] whereas in $ZnMn_2O_4$, they are detected at 300, 321, 382, 475 and 678 cm^{-1}, respectively.[106] As a general behavior, the band positions decrease with the increase of the radii of both octahedral and tetrahedral cations,[95] *e.g.* in aluminate spinels, the position of the E_g mode downshifts with increasing radius of tetrahedral cation (from 411 cm^{-1} in $ZnAl_2O_4$ to 395 cm^{-1} in $MnAl_2O_4$);[95] the same occurs in chromites for the position of the $F_{2g}(2)$ mode (which moves from 541 cm^{-1} in $MgCr_2O_4$ to 492 cm^{-1} in $FeCr_2O_4$).[95] As a general behavior, the band positions decrease with the increase of the radii of both octahedral and tetrahedral cations.[95] The partial substitution of either divalent or trivalent cations with different divalent and trivalent cations, respectively, reflects in changes (in the lattice parameters and) in the spectral profile, with shifts of the Raman peaks and variations of their relative intensities.[98,107] Other factors, such as the nanoparticle size[108] and the presence of defect-induced lattice distortions,[103] are also influential.

In the present case, by comparing the spectra of the three samples (Fig. 6), no marked differences in apparent positions and relative intensities of the peaks are noticed below 400 cm^{-1}, which hints to a larger involvement of the trivalent cations[99,101,103] (Cr^{3+}, Mn^{3+}, Fe^{3+}, present in all samples) in the weaker $F_{2g}(1)$ and E_g modes. On the contrary, above 400 cm^{-1}, the spectral profiles are clearly different, pointing to a greater sensitivity of the stronger $F_{2g}(2)$, $F_{2g}(3)$ and A_{1g} modes to the change in composition of the HEO-NFs (*i.e.* to the substitution of one of the divalent cations). In Ni-containing CoNi and NiZn NFs, the $F_{2g}(2)$ mode (apparently peaking between 504 and 517 cm^{-1}) is better resolved than in CoZn NFs, where it appears as a shoulder (at ~500 cm^{-1}), while the most intense A_{1g} mode, lying in the frequency range (620–700 cm^{-1}) peculiar to ferrites and chromites,[102,104] apparently peaks at 658 cm^{-1} in NiZn NFs and at lower frequencies (633 and 620 cm^{-1}) in CoZn and CoNi NFs. In the latter sample, a shoulder further appears on the higher frequency side of the A_{1g} mode, suggesting the occurrence of inversion,[71,95,109] in agreement with what reported for $(Cr_{1/5}Mn_{1/5}Fe_{1/5}Co_{1/5}Ni_{1/5})_3O_4$ nanoparticles, prepared *via* sol–gel method[43] and reverse co-precipitation approach.[76]

To ensure electroneutrality of the 2–3 spinel M_3O_4 phase, 1/3 of the cations must have charge +2 and 2/3 must have charge +3. Considering the relative stability of M^{2+} and M^{3+} cations in the spinel oxide lattice it is expected that chromium and zinc are present as Cr^{3+} and Zn^{2+}, respectively. The other cations (Mn, Fe, Co, Ni) can occur as both M^{2+} and M^{3+}. The preference for M^{3+} decreases as Mn > Fe > Co > Ni.

In spinel oxides, cations occupy tetrahedral 8a sites and octahedral 16d sites (Fig. S1, ESI†). The energy difference between the 8a and 16d site for middle-late 3d ions ranges from 0 (d^5 and d^{10} ions) to 158 kJ mol^{-1} (d^3 Cr^{3+}).[110,111] This explains why ferrites MFe_2O_4 are often inverse (Fe^{3+} is d^5), while

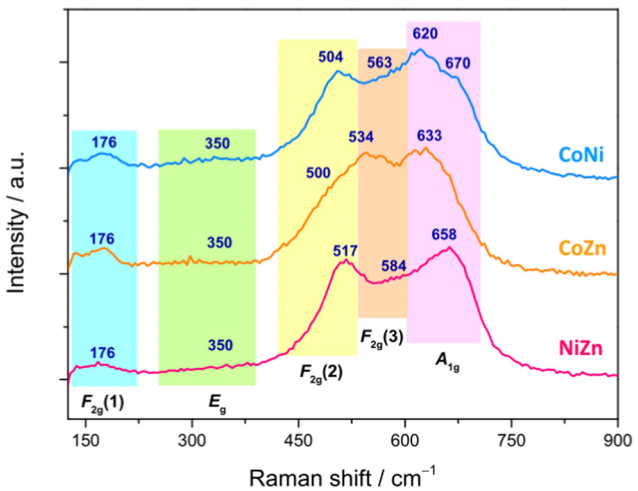

Fig. 6 Averaged micro-Raman spectra of the HESO-NFs (the apparent peak positions, in cm^{-1}, are also reported).

chromites MCr_2O_4 are always normal.[112] Clearly, TEM is not able to resolve the 8a and 16d sites, so one may wonder whether entropic effects are strong enough to overcome the cation site preferences and achieve uniform cation distribution over all sites, or uniform distribution only occurs within 8a and 16d sites separately, leaving room to satisfy the cation site preferences. Using the crystal-field-theory based values for the octahedral stabilization energy[110] and adapting the formula for the configurational entropy[113] of a crystal with sublattice to the spinel structure as

$$S_{\text{config}}^{\text{FU}} = -R\left(\sum_i x_i^{(8a)} \ln x_i^{(8a)} + 2\sum_i x_i^{(16d)} \ln x_i^{(16d)}\right) \quad (1)$$

where the configurational entropy is calculated for a formula unit (FU) M_3O_4, $x_i^{(8a)}$ and $x_i^{(16d)}$ are the fractions of metal i occupying the 8a and 16 sites, respectively, we can estimate the Helmoltz free energy F^{FU} corresponding to a given distribution of cations. The distributions are strongly favored that have cations (i) partitioned between 8a and 16d sites to optimize octahedral stabilization, and (ii) randomly distributed within the 8a and 16d sites, under the electroneutrality constraint. At 1173 K (our highest calcination temperature), the cation distributions detailed in Table 1 have F^{FU} lower than that of the completely random distribution by 37 to 45 kJ mol^{-1} (the details of the calculations can be found in the ESI†). The occurrence of intrasite-random cation distributions is consistent with the presence of Mn as Mn^{3+}, Fe as a mixture of Fe^{2+} and Fe^{3+}, and of Co mostly as Co^{2+}, evidenced by the XPS data. It also agrees with the XAS data for $(Co_{1/5}Mg_{1/5}Mn_{1/5}Ni_{1/5}Zn_{1/5})$-$(Al_{1/5}Co_{1/5}Cr_{1/5}Fe_{1/5}Mn_{1/5})_2O_4$,[114] and the XANES data for $(Ti_{1/5}Mn_{1/5}Fe_{1/5}Co_{1/5}Ni_{1/5})_3O_4$,[115] which indicate that the cation site preferences are satisfied. Very recently, Sarkar *et al.*[65] demonstrated that micrometer-sized $(Cr_{1/5}Mn_{1/5}Fe_{1/5}Co_{1/5}Ni_{1/5})_3O_4$ HESO has intrasite-random cation distribution with $(Co_{3/5}Fe_{2/5})$ in 8a sites and $(Cr_{3/5}Mn_{3/5}Fe_{1/5}Ni_{3/5})$ in 16d sites using X-ray, Mössbauer, and neutron techniques. They also expect that Cr and Fe are present as trivalent cations, Ni as divalent cation, and Mn and Co as a mixture of M^{2+} and M^{3+} (M^{2+}/M^{3+} = 10 : 90 for Mn, 60 : 40 for Co). The important role of the excess octahedral stabilization was recognized, as we independently did. The data are close to those in Table 1. So, we are confident that the cation distributions we propose for $(Cr_{1/5}Mn_{1/5}Fe_{1/5}Co_{1/5}Zn_{1/5})_3O_4$ and $(Cr_{1/5}Mn_{1/5}Fe_{1/5}Ni_{1/5}Zn_{1/5})_3O_4$ are close to the true ones.

Table 1 Cation distributions that satisfy electroneutrality and optimize octahedral stabilization

NF	Site	M^{2+}	M^{3+}	λ^a (%)
CoNi	8a	$Co_{1/5}$	$Fe_{3/5}Co_{1/5}$	80
	16d	$Ni_{3/5}Co_{1/5}$	$Cr_{3/5}Mn_{3/5}$	
CoZn	8a	$Zn_{3/5}$	$Fe_{2/5}$	40
	16d	$Co_{2/5}$	$Cr_{3/5}Mn_{3/5}Fe_{1/5}Co_{1/5}$	
NiZn	8a	$Zn_{3/5}$	$Fe_{2/5}$	40
	16d	$Ni_{2/5}$	$Cr_{3/5}Mn_{3/5}Fe_{1/5}Ni_{1/5}$	

[a] Inversion degree, defined as the fraction of trivalent cations in the 8a sublattice.

In order to infer additional information, Gaussian bands were utilized to reproduce the micro-Raman spectra (Fig. S10, ESI†). Besides the $F_{2g}(1)$, E_g, $F_{2g}(2)$, $F_{2g}(3)$ and A_{1g} modes, additional bands were found to contribute to the Raman intensity, confirming that inversion occurs, to different extent, in all samples.[71,76,95,109]

Magnetic properties

General considerations. It is clear from the preceding discussion that the interpretation of the magnetic data will benefit from reference to chromites, manganites, and ferrites with spinel structure.

The primary particles comprising the HESO-NFs have diameter from a few tens of nm to the hundred nm range. From XRD data, the average crystallite diameter is ≈100 nm for CoNi and NiZn and ≈85 nm for CoZn. Magnetic lengths, such as the single-domain, coherent rotation, and superparamagnetic (SPM) blocking diameters,[116] are a useful (though approximate) starting framework to develop the interpretation of magnetic data. We could find in the literature data for Fe_3O_4, $CoFe_2O_4$, and $CoCr_2O_4$ (Table S8, ESI†). The NF primary particles have diameter similar to the single-domain diameter of Fe_3O_4 and much smaller than that of $CoFe_2O_4$ and $CoCr_2O_4$, so they reasonably comprise a single domain. Magnetization inversion by coherent rotation diameter is expected if the NF behave as chromites but partially incoherent inversion (*e.g.*, curling) might occur if the NFs behave similarly to ferrites. Finally, the NF primary particles are much larger than the SPM blocking diameter at 400 K of all three spinel oxides and, therefore, superparamagnetism is not expected to be important.

Magnetic data and analysis. The high field magnetization M_{50k} (H = 50 kOe) and remanence M_{rem} were measured between 5 and 300 K (Fig. 7). All samples have significant high-field and remanent magnetization, at least at low temperature, and are thus able to sustain a magnetically ordered structure. M_{50k} and M_{rem} at 5 K are in the 17–40 emu g^{-1} and 10–30 emu g^{-1} range, respectively, that correspond to molar magnetization per formula unit (FU) in the range 0.7–1.7μ_B and 0.4–1.3μ_B, respectively (μ_B is the Bohr magneton). Since the cations, except Zn^{2+}, have molar magnetization in the 3.2–5.9μ_B range, the measured M_{50k} and M_{rem} demonstrate that the NFs have an ordered magnetic structure of ferrimagnetic (FIM) nature, excluding ferromagnetic (FM) and (canted) antiferromagnetic (AFM) structures, which would display much larger and smaller M_{50k} and M_{rem}, respectively. The squareness M_{50k}/M_{rem} is large at 5 K, it extrapolates to ≈0.75 at 0 K, a value typical of Stoner–Wohlfarth particles with cubic anisotropy. Incoherent magnetization inversion and interparticle interactions seem thus to be relatively unimportant even at low temperature.[117]

The magnetization for a completely collinear FIM structure, such as that found in the mixed ferrites MFe_2O_4, can be calculated by a Monte Carlo approach based on Table 1. The calculated values are 2.5, 7.0, 6.3μ_B per FU for CoNi, CoZn and NiZn NFs, respectively. Thus, the observed magnetization is not

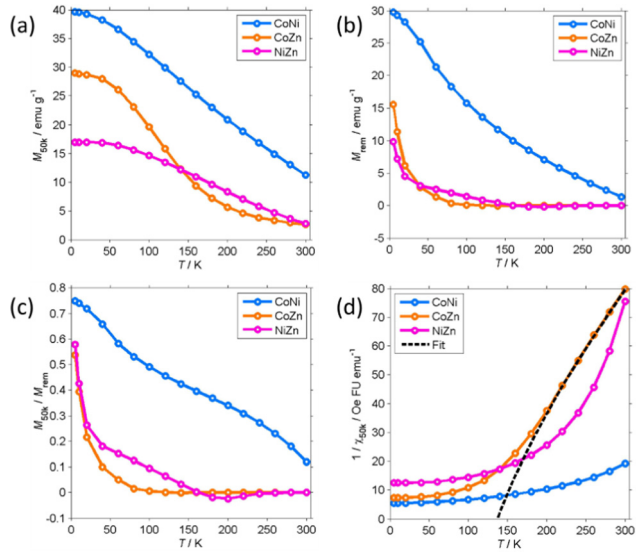

Fig. 7 Temperature dependence of the high field magnetization M_{50k} (a, H = 50 kOe), remanence M_{rem} (b), squareness M_{50k}/M_{rem} (c), and inverse high-field susceptibility $1/\chi_{50k}$ (d) of the NFs. The dashed line in panel (d) is the best-fit Curie–Weiss–Néel curve for CoZn NFs.

consistent with a collinear, antiparallel alignment of the ionic magnetic moments (sublattice magnetizations), like in the typical Néel FIM structure. It is however consistent with a FIM structure where the sublattice magnetizations are not collinear.

M_{50k} and M_{rem} decrease with increasing temperature. M_{rem} of CoNi at 300 K (1.35 emu g^{-1}) is 5% of the remanence at 5 K. The remanence of Zn-containing (CoZn and NiZn) NFs vanishes well below RT. Therefore, CoZn and NiZn NFs are paramagnetic (PM) at 300 K and CoNi NFs probably becomes PM slightly above RT.

We now turn our attention to the transition temperature T_C between the FIM and PM phases. Considering that the primary particles have size ranging from a few tens of nm to the hundred nm range, we expect a distribution of transition temperatures. The temperature, at which M_{rem} vanishes, marks the T_C of the primary particles with highest T_C, presumably the largest particles. Due to noise and artifacts, it is not possible to accurately measure where M_{rem} vanishes. The best estimate is that $T_C \approx 150$ and 200 K for CoZn and NiZn NFs, respectively. This ordering of the T_C = (CoNi > NiZn > CoZn) can also be appreciated in the M_{50k} plot (Fig. 7). M_{50k} of CoZn changes concavity at ≈150 K, suggesting that at higher temperatures it follows the Curie–Weiss–Néel law for ferrimagnets,[112]

$$\frac{1}{\chi} = \frac{T}{C} + \frac{1}{\chi_0} - \frac{\sigma}{T - \theta_p} \quad (2)$$

where $\chi = M/H$ is the susceptibility, C is the Curie constant, χ_0 and σ are related to the intra- and inter-sublattice molecular fields, and θ_p is the paramagnetic Curie point, which is slightly higher than the true transition temperature T_C.[118] As can be seen in Fig. 7d, $1/\chi_{50k}$ of CoZn closely follows the Curie–Weiss–Néel law for $T > 200$ K, so we can identify the PM and FIM Curie points $T_C \approx \theta_p = 137$ K, in agreement with T_C from M_{rem} data. Interestingly, the asymptotic temperature $\theta_N = -C/\chi_0$ is close to zero, indicating the presence of frustrated FM and AFM exchange interactions that compete and partly compensate.[119] The Curie constant corresponds to an effective moment $\mu_{eff} = (3k_BC/N_A) = 5.0\mu_B$ per FU that is just 66% of that calculated by a Monte Carlo approach. This discrepancy is probably due to the lack of data in the high temperature range where the T/C term of eqn (2) is dominant.

Confirmation of the presence of a FIM-PM transition and details about the FIM phase are provided by the magnetization isotherms $M(H)$ measured at different temperature (Fig. 8). Since the magnetization is not always saturated at 50 kOe, we analyzed how M approaches saturation[117] to more accurately estimate the true M_{sat}.

The magnetic parameters are collected in Table 2 (see Experimental section in ESI† for details).

The behavior of the NFs is markedly different from each other. The CoNi NFs have open loops that do not change shape up to 300 K. At low T, the coercivity H_c is moderate (0.83 kOe). On increasing temperature, M_{sat}, M_{rem}, H_c, and the coercivity of the remanence H_{cr} decrease slowly due to the approach to the

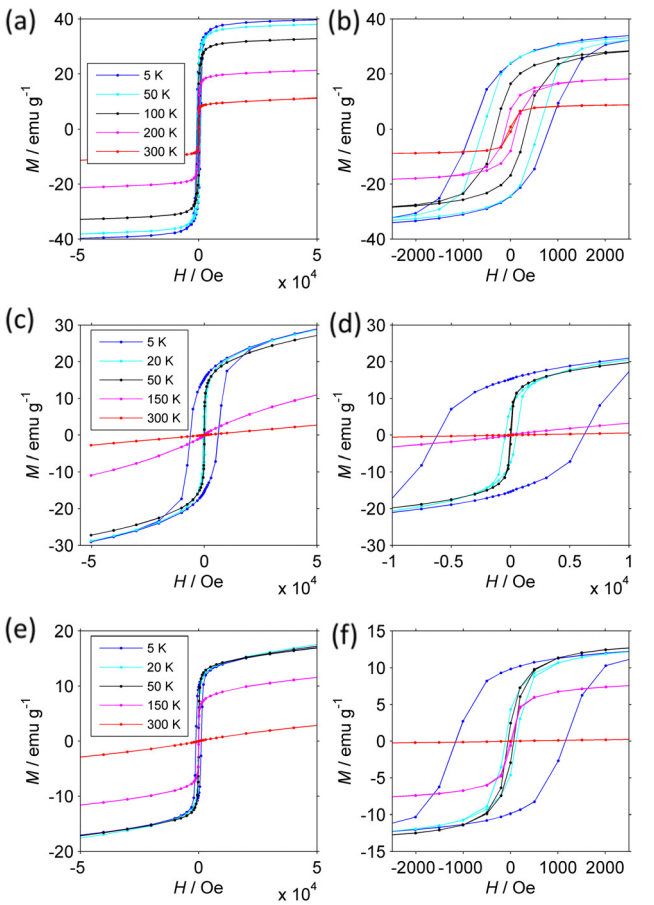

Fig. 8 Magnetization isotherms $M(H)$ of the (a and b) CoNi, (c and d) CoZn and (e and f) NiZn NFs. The panels (b, d and f) show the central part of the isotherms. Note the different horizontal scale of the panel (d).

critical FIM-PM T_C. This interpretation is supported by the large size of the primary particles and the dependence of coercivity on T. Indeed, neither H_c nor H_{cr} follow Kneller's law[120] typical of thermally activated magnetization inversion process. They instead follow a power law $(H_c/H_{c,0}) \approx (M_{sat}/M_{sat,0})^{4.5}$, where the 0 subscript indicates the value at 5 K, which, provided that H_c is proportional to the anisotropy field 2 K/M_{sat}, is consistent with Zener's law[121] typical of bulk materials. Further supporting evidence will be provided below.

The magnetization isotherms of CoZn and NiZn NFs have similar behavior though at shifted temperature mirroring the different T_C. From 5 to 150 K, they are open loops with almost constant M_{sat} and dramatically decreasing H_c (and H_{cr}). The main difference is that CoZn NFs have much larger H_c at 5 K (6.37 kOe) than NiZn NFs have (1.17 kOe). It is noteworthy that CoNi NFs have H_c lower than that of CoZn NFs, despite the presence of Co in both NFs. This difference can be attributed to the fact that in CoZn NFs a larger fraction of Co is present in octahedral 16d sites (see Table 1). At 150 K, the magnetization of NiZn NFs still is non-linear, while that of CoZn NFs is almost linear. At 300 K, both NFs are definitely in a linear regime: at H = 50 kOe, the paramagnetic magnetization $M_p = \chi_p H$ is 83% and 99% of the total M_{50k} magnetization for NiZn and CoZn NFs, respectively. M_p is truly related to primary particles that have entered the PM regime, as shown by the small magnitude of its slope χ_p, which corresponds to a magnetization of a few μ_B per FU. In the SPM regime, the initial susceptibility would be several orders of magnitude larger and strong non-linearity would be observed already at $H < 1$ kOe.

Temperature dependent $M(H)$ curves have thus strengthened the conclusion that our HESO-NFs have a low-T FIM phase and a high-T PM phase with transition temperature T_C decreasing as CoNi > NiZn > CoZn. They have provided further evidence that SPM effects are not dominant, as anticipated on the basis of the size of the primary particles. The small χ_p, corresponding to a FU magnetization of a few μ_B, is consistent with a non-collinear FIM structure.

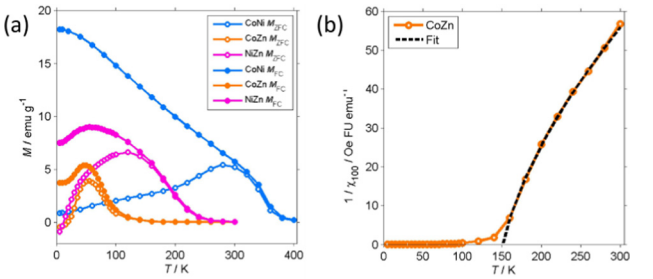

Fig. 9 Temperature dependence of the low-field (100 Oe) magnetization of the NFs. Left: ZFC and FC magnetization of the NFs. Right: Inverse low-field susceptibility $1/\chi_{100}$ of CoZn NFs. The dashed line is the best-fit Curie–Weiss–Néel curve for CoZn NFs.

More detailed information about the magnetic structure of the NFs is obtained from the zero-field cooled (ZFC) and field cooled (FC) magnetization (M_{ZFC}, M_{FC}) measured with H_{cool} = H_{meas} = 100 Oe (Fig. 9). All (Z)FC curves differ from the typical (Z)FC curves of ferrite NPs.

For instance, the ZFC–FC bifurcation occurs at temperature much higher than the maximum M_{ZFC}. The NFs display (Z)FC curves with similar shape that have different temperature span in correspondence to the unequal T_C. Extending the temperature range up to 400 K allowed us to observe the transition of CoNi NFs to the PM phase. There clearly is a dispersion of the transition temperature due to the particulate nature of the NFs.

Therefore, to estimate T_C from M_{FC} data, the intercept of the maximum slope line was extrapolated and its intersection with the M = 0 axis was interpreted as an average T_C. For CoNi NFs, the FIM-PM transition occurs at T_C = 374 K (Table 3). On decreasing T, M_{FC} increases almost linearly and then levels off at $T \leq 20$ K. No low T transition is observed. The M_{FC} of CoNi NFs is almost exactly proportional to M_{50k} ($M_{FC} \approx 0.44 M_{50k}$) showing that there is a common thermal process underlying the M increase at low T. This process is the thermal dealignment of the spins about the magnetization axis. Thermally activated magnetization inversion (superparamagnetism) can be excluded since it strongly depends on the applied field. The large difference between M_{ZFC} and M_{FC} may be related to several causes.

It can be due to the presence of sizeable magnetic anisotropy typical of spinel oxides. The power dependence of H_c on M_{sat} supports this hypothesis. Another possible explanation is the

Table 2 Magnetic parameters of the NFs calculated from the magnetization isotherms $M(H)$. Parameters may be absent when the NFs are mostly paramagnetic

	T (K)	M_{sat}[a] (emu g^{-1})	M_{rem} (emu g^{-1})	M_{rem}/M_{sat}	H_c (kOe)	H_{cr} (kOe)	$10^4\ \chi_p$ (emu g^{-1} Oe^{-1})
CoNi	5	39.3	24.1	0.61	0.82	0.94	0.15
	50	37.4	24.2	0.64	0.59	0.70	0.18
	100	31.9	16.6	0.52	0.32	0.35	0.22
	200	20.0	7.6	0.38	0.11	0.14	0.28
	300	9.6	0.9	0.09	0.02		0.36
CoZn	5	27.9	15.3	0.55	6.37	6.77	0.72
	20	23.4	7.2	0.31	0.48	0.68	1.23
	50	21.8	1.97	0.09	0.04	0.04	1.22
	150	3.68	0.02	0.006	0.03		1.55
	300						0.54
NiZn	5	14.8	9.86	0.65	1.17	1.30	0.51
	20	14.7	4.47	0.30	0.12	0.17	0.62
	50	14.6	2.69	0.18	0.06	0.09	0.57
	150	9.6	0.35	0.04	0.01		0.44
	300	0.7			0.01		0.45

[a] M_{sat} is the saturation magnetization as obtained from the analysis of the approach to saturation.[117]

Table 3 Critical temperatures of the NFs[a]

NF	T_C (K)	T_S (K)
CoNi	374	
CoZn	105	20
NiZn	233	11

[a] Estimated from the intercept of the maximum slope line with the M = 0 axis (T_C) or $M = M$(5 K) line (T_S).

formation of a spin-glass-like phase below RT. This seems less likely, at least for CoNi, as M_{ZFC} and M_{FC} are already unequal at RT.

The (Z)FC magnetization of Zn-containing NFs is close to zero at RT and rapidly increases when the transition to the FIM phase approaches. The PM phase gives way to a FIM phase at T_C = 233 (NiZn) and 105 K (CoZn), temperatures much lower than that of CoNi NFs. M_{FC} reaches a maximum at 50 K and then decreases and levels off at low T. This marks the transition to a phase with lower M at the (average) critical temperature T_S = 11 and 20 K for NiZn and CoZn NFs, respectively. The M decrease suggests the formation of a spin-glass-like phase. The shape of M_{ZFC} does not allow us to exclude SPM phenomena, but the thermal unblocking of the spin-glass-like phase and the thermal decrease of M_{sat} (clearly observed in the CoNi NFs) seems sufficient to explain the temperature dependence of M_{ZFC}. Therefore, the (Z)FC magnetization of Zn-containing NFs gives evidence of the occurrence of another magnetic structure at very low T.

The low-field susceptibility $\chi_{100} = M_{FC}/H_{meas}$ sufficiently extends above T_C to be significantly modelled by the Curie–Weiss–Néel law (eqn (2)) only for the CoZn NFs. $1/\chi_{100}$ closely follows eqn (2) for $T > 150$ K (Fig. 9). The asymptotic temperature $\theta_N \approx 0$ and the effective moment $\mu_{eff} = 6.1\mu_B$ (80% of μ_{eff} calculated by a Monte Carlo approach) are both in agreement with the results of the modelling of $1/\chi_{50k}$. The best-fit parameters provide $T_C \approx \theta_p = 150$ K, in agreement with M_{rem} data and the modeling of the high-field susceptibility. This T_C is not inconsistent with that in Table 3 since the former is the T_C of the largest particles while the latter represent an average over all particles.

Discussion of the magnetic properties and structure

As anticipated, the magnetic results can be discussed with reference to the magnetic structure of ferrites, chromites, and manganites. The magnitude of M_{sat} and the temperature dependence of $M_{(Z)FC}$ and H_c are not consistent with the usual behavior of ferrites, which have Néel FIM phases with collinear sublattice magnetization and T_C above $\approx$600 K. It is also interesting to note that when Zn replaces a magnetic cation (Co, Ni) in our NFs, the magnetization decreases, at variance with ferrites that show the well-known magnetization increase upon Zn substitution.[122]

In spinel-structure chromites MCr_2O_4 and manganites MMn_2O_4, the interplay between strength and frustration of the superexchange interactions is such that they display a non-collinear FIM phase with M_{sat} and T_C much lower than those the of corresponding ferrites MFe_2O_4, and often a transition (T_S) to a low temperature reentrant spin-glass-like phase.[119] The magnetic structure of the low-T phase in chromites typically is conical/spiral with a long-range ordered longitudinal component and a short-range (a few nm) ordered transverse component.[123–125] The low-T phase of manganites has been less studied. The neutron diffraction data of $NiMn_2O_4$ at T = 1.5 K were interpreted in terms of a strongly canted magnetic structure where the sublattice magnetizations form an angle of 27°.

The magnetic behavior of Zn-containing CoZn and NiZn NFs closely resembles that of chromite (and manganites) under many respects. For instance, the dramatic decrease of coercivity at low T indicates the transition between the spin-glass-like and the non-collinear FIM phase.[126] Therefore, the magnetic behavior of CoZn and NiZn NFs is consistent with the presence of an intermediate non-collinear FIM phase and a low-T reentrant spin-glass-like phase. The CoNi NFs share some magnetic characteristic with chromites, *e.g.*, the low M_{sat}, but under other respects, *e.g.*, the relatively high T_C and the slow decrease of M_{sat}, M_{rem}, and H_c with increasing T, they behave like a ferrite. This behavior can be understood with reference to the parameter u,[126] which quantifies the magnetic frustration:

$$u = (4J_{BB}S_B)/(3J_{AB}S_A) \quad (3)$$

where J_{AB} is the superexchange integral between the nearest-neighbor spins at the 8a and 16d sites, J_{BB} is that between the nearest-neighbor spins at two 16d sites, and S_A and S_B are the magnitudes of the spins at the 8a and 16d sites. For small u ($< 8/9$), Néel collinear FIM structure occurs, but at larger u the increasing frustration gives rise to non-collinear FIM structures with decreasing order range.[123] In CoNi the full network of superexchange interactions counteracts the magnetic frustration and the effects of the latter are weaker than those in MCr_2O_4 and MMn_2O_4 spinel oxides. The replacement of a magnetic cation by Zn^{2+} in CoZn and NiZn NFs significantly reduces the average values of both J_{AB} and S_A, leading to a lower T_C, and it increases u and the magnetic frustration, leading to lower collinearity and the occurrence of a reentrant spin-glass-like-phase at low T.

The above argument about magnetic structure is based on the close similarities of the chemical composition, crystal structure, and magnetic behavior between our HESO NFs and the spinel oxides chromites, manganites, and ferrites. Of course, we do not claim that we have proved the HESO NF magnetic structure, which would require additional experiments, such as magnetic neutron scattering, that are outside the scope of this paper. It however seems more likely that, for compounds of identical crystal structure and similar chemical composition, similar magnetic behavior stems from similar magnetic structure than that different magnetic structures accidentally give rise to similar magnetic behavior. Caution is however in order as HE compounds might display properties far from those of the corresponding low-entropy compounds.

Finally, we compare our results with preceding magnetic characterization of HESOs. The magnetic properties of HESOs have already been summarized.[59,60] Spinel oxides with composition $(Cr_{1/5}Mn_{1/5}Fe_{1/5}Co_{1/5}Ni_{1/5})_3O_4$, equal to that of CoNi NFs, have attracted some attention. The literature magnetic data (Table 4) are in general agreement with those recorded for our CoNi NFs but they were rarely discussed in detail. Magnetization isotherms were first measured on NP aggregates obtained by solution combustion followed by calcination.[64,127] The $M(H)$ curves at RT were slightly open loops similar to that of CoNi NFs. $M(H)$ at 300 K was also measured on aggregates of $\approx$100 nm particles synthesized by a sol–gel procedure, and in this case a closed $M(H)$ curve typical of SPM behavior was recorded.[63] A more in-depth investigation of bulk $(Cr_{1/5}Mn_{1/5}Fe_{1/5}Co_{1/5}Ni_{1/5})_3O_4$ obtained by sintering at 1273 K was later reported.[65] The results

Table 4 Magnetic parameters of HESOs from the literature

	T (K)	High-field M (emu g^{-1})	M_{rem} (emu g^{-1})	H_c (kOe)	T_C (K)	Ref.
$(Cr_{1/5}Mn_{1/5}Fe_{1/5}Co_{1/5}Ni_{1/5})_3O_4$	RT	16.0[a]	3.8	0.06		127
	RT	9.9[b]	2.5	0.18		64
	300	16[c]				63
	4	44[d]	21	0.51	412,[e] 435[f]	65
	300	13.2[c]		0.02		62
	50	35.3[c]		0.20		
	300	41.1[g]			>380 K	65
	5	15.9[g]		0.23		
$(Cr_{1/5}Mn_{1/5}Fe_{1/5}Co_{1/5}Zn_{1/5})_3O_4$	RT	8.1[b]	0.8	0.06		64
$(Cr_{1/5}Mn_{1/5}Fe_{1/5}Ni_{1/5}Zn_{1/5})_3O_4$	RT	5.6[b]	0.6	0.09		64

[a] At 20 kOe. [b] At 30 kOe. [c] At 5 kOe. [d] At 90 kOe. [e] From magnetization data. [f] From Mössbauer data. [g] At 40 kOe.

from Mössbauer and magnetometric data, including the FIM-PM T_C, are very similar to those of CoNi NFs. A broad investigation of high-entropy spinel oxides M_3O_4, ferrites MFe_2O_4, and chromites MCr_2O_4 has been reported upon, which includes $(Cr_{1/5}Mn_{1/5}Fe_{1/5}Co_{1/5}Ni_{1/5})_3O_4$, spinel oxide.[62] The HEOs were synthesized by ball milling, compression, and sintering at 1523 K. The $M(H)$ isotherms (5–300 K) of $(Cr_{1/5}Mn_{1/5}Fe_{1/5}Co_{1/5}Ni_{1/5})_3O_4$ are consistent with the present data for CoNi NFs, but the M_{ZFC} and M_{FC} curves are rather different. The latter have a shape loosely similar to the curves in Fig. 9, but they are quantitatively very different, *e.g.*, M_{FC} (5 K, H_{cool} = H_{meas} = 100 Oe) for the bulk HESO (6.6 emu g^{-1}) unexpectedly is much lower than that of CoNi NFs (18.2 emu g^{-1}). The magnetic data was explained in terms of the occurrence of Cr or Mn rich regions with AFM structure. We think that the behavior of $(Cr_{1/5}Mn_{1/5}Fe_{1/5}Co_{1/5}Ni_{1/5})_3O_4$ HESO is better explained on the basis of the presence of Cr and Mn, reasonably as Cr^{3+} and Mn^{3+} in the 16d sites. Indeed, in the same paper the ZFC–FC curves of high-entropy chromites MCr_2O_4 are displayed, which closely resemble those of the CoZn and NiZn NFs and confirm that frustration effects are induced by Cr and increased by the replacement of magnetic cations by non-magnetic ones. Finally, micrometer-sized $(Cr_{1/5}Mn_{1/5}Fe_{1/5}Co_{1/5}Ni_{1/5})_3O_4$ particles were recently studied.[65] The 300 K isotherm is reversible whereas at 5 K a small coercivity (0.23 kOe) was observed. These data agree with those here measured for CoNi NFs, the coercivity difference is explained by the larger size of the particles, which are multidomain (see Table S8, ESI†). The (Z)FC magnetization is similar to the present one except for an inflection at $\approx$75 K, which was attributed to the depinning of domain walls.

HESOs with composition equal to CoZn and NiZn NFs have been much less studied.[64] The RT $M(H)$ curves of aggregates of 24 nm NPs, obtained by solution combustion followed by calcination, were slightly open loops (H_c < 0.1 kOe) in stark contrast with CoZn and NiZn NFs, which are essentially PM at RT. We can only speculate that this striking difference is due the different synthetic route and morphology of the oxides.

Conclusions

Electrospun $(Cr_{1/5}Mn_{1/5}Fe_{1/5}Co_{1/5}Ni_{1/5})_3O_4$, $(Cr_{1/5}Mn_{1/5}Fe_{1/5}Co_{1/5}Zn_{1/5})_3O_4$ and $(Cr_{1/5}Mn_{1/5}Fe_{1/5}Ni_{1/5}Zn_{1/5})_3O_4$ NFs, exhibit porous structure consisting of interconnected nearly strain-free oxide single crystals with pure $Fd\bar{3}m$ spinel structure. The in-depth investigation of their magnetic properties shows that $(Cr_{1/5}Mn_{1/5}Fe_{1/5}Co_{1/5}Ni_{1/5})_3O_4$, $(Cr_{1/5}Mn_{1/5}Fe_{1/5}Co_{1/5}Zn_{1/5})_3O_4$ and $(Cr_{1/5}Mn_{1/5}Fe_{1/5}Ni_{1/5}Zn_{1/5})_3O_4$ NFs have a diverse and rich magnetic behavior, grounded into the random cation distribution within (but not across) sublattices. In particular, the Zn-containing NFs display complex magnetic structures at low temperature. The substitution of a single cation (20% of the cationic content) changes the FIM-PM T_C by about 130 K. More insight into this fascinating magnetism could be obtained by investigating the details of the cation distribution, as recently carried out for $(Cr_{0.2}Mn_{0.2}Fe_{0.2}Co_{0.2}Ni_{0.2})_3O_4$.[65] Furthermore, the suggested magnetic structure of our HESO NFs should be proved by direct techniques such as neutron diffraction. Of course, the randomness inherent in HEMs makes such detailed investigations a difficult endeavor.

Author contributions

Conceptualization, A. P. and S. S.; methodology, C. T., B. P., A. M. F., G. P., V. D. N. and X. W.; validation and formal analysis, C. T., A. M. F., G. P. and V. D. N.; data curation, A. P., C. T., A. M. F., G. P., V. D. N. and S. S.; writing—original draft preparation, A. P. and S. S.; writing—review and editing, A. P., N. P. and S. S. All authors have read and agreed to the published version of the manuscript.

Conflicts of interest

There are no conflicts to declare.

Acknowledgements

We thankfully acknowledge Christoph Erdmann for electron microscopy measurements and Mauro Coduri for his help in the Rietveld analysis. A. P. and A. M. F. are grateful to ERA and MUR for funding the ERA-MIN3 project Rendering3D (Reference Number: JTC-2021_207). The research at the University of Padova has received funding from the Italian Ministry of University and Research with the FISR 2019 project ''Alkaline membranes and (platinum group metals)-free catalysts

enabling innovative, open electrochemical devices for energy storage and conversion – AMPERE'' (Project number FISR2019_01294). W. X. acknowledges the fellowship from the China Scholarship Council (CSC).

Notes and references

1 B. Cantor, I. T. H. Chang, P. Knight and A. J. B. Vincent, *Mater. Sci. Eng., A*, 2004, **375**, 213A–218A.
2 J. W. Yeh, S. K. Chen, S. J. Lin, J. Y. Gan, T. S. Chin, T. T. Shun and S. Y. Chang, *Adv. Eng. Mater.*, 2004, **6**(5), 299–303.
3 G. Zhang, K. Ming, J. Kang, Q. Huang, Z. Zhang, X. Zheng and X. Bi, *Electrochim. Acta*, 2018, **279**, 19–23.
4 R. Q. Yao, Y. T. Zhou, H. Shi, W. B. Wan, Q. H. Zhang, L. Gu and Q. Jiang, *Adv. Funct. Mater.*, 2021, **31**(10), 2009613.
5 D. Feng, Y. Dong, P. Nie, L. Zhang and Z. A. Qiao, *Chem. Eng. J.*, 2022, **430**, 132883.
6 T. X. Nguyen, Y. C. Liao, C. C. Lin, Y. H. Su and J. M. Ting, *Adv. Funct. Mater.*, 2021, **31**(27), 2101632.
7 J. Hu, L. Cao, Z. Wang, J. Liu, J. Zhang and Y. Cao, *et al.*, *Compos. Commun.*, 2021, **27**, 100866.
8 F. Liu, M. Yu, X. Chen, J. Li, H. Liu and F. Cheng, *Chin. J. Catal.*, 2022, **43**(1), 122–129.
9 N. L. Broge, M. Bondesgaard, F. Søndergaard-Pedersen, M. Roelsgaard and B. B. Iversen, *Angew. Chem.*, 2020, **132**(49), 22104–22108.
10 A. Sarkar, L. Velasco, D. Wang, Q. Wang, G. Talasila and L. de Biasi, *et al.*, *Nat. Commun.*, 2018, **9**(1), 3400.
11 A. Amiri and R. J. Shahbazian-Yassar, *Mater. Chem. A*, 2021, **9**(2), 782–823.
12 M. Fu, X. Ma, K. Zhao, X. Li and D. Su, *iScience*, 2021, **24**(3), 102177.
13 I. Hussain, C. Lamiel, M. Ahmad, Y. Chen, S. Shuang and M. S. Javed, *et al.*, *J. Energy Storage*, 2021, **44**, 103405.
14 D. Bérardan, S. Franger, A. K. Meena and N. J. Dragoe, *Mater. Chem. A*, 2016, **4**(24), 9536–9541.
15 Q. Wang, A. Sarkar, D. Wang, L. Velasco, R. Azmi and S. S. Bhattacharya, *et al.*, *Energy Environ. Sci.*, 2019, **12**(8), 2433–2442.
16 Y. Chen, H. Fu, Y. Huang, L. Huang, X. Zheng and Y. Dai, *et al.*, *ACS Mater. Lett.*, 2020, **3**(2), 160–170.
17 H. Chen, N. Qiu, B. Wu, Z. Yang, S. Sun and Y. Wang, *RSC Adv.*, 2019, **9**(50), 28908–28915.
18 P. Ghigna, L. Airoldi, M. Fracchia, D. Callegari, U. Anselmi-Tamburini and P. D'angelo, *et al.*, *ACS Appl. Mater. Interfaces*, 2020, **12**(45), 50344–50354.
19 S. Y. Wang, T. Y. Chen, C. H. Kuo, C. C. Lin, S. C. Huang and M. H. Lin, *et al.*, *Mater. Chem. Phys.*, 2021, **274**, 125105.
20 N. Qiu, H. Chen, Z. Yang, S. Sun, Y. Wang and Y. Cui, *J. Alloys Compd.*, 2019, **777**, 767–774.
21 A. J. Wright and J. J. Luo, *Mater. Sci.*, 2020, **55**(23), 9812–9827.
22 C. Oses, C. Toher and S. Curtarolo, *Nat. Rev. Mater.*, 2020, **5**(4), 295–309.
23 R. Z. Zhang, F. Gucci, H. Zhu, K. Chen and M. J. Reece, *Inorg. Chem.*, 2018, **57**(20), 13027–13033.
24 Y. Qin, J. X. Liu, F. Li, X. Wei, H. Wu and G. J. Zhang, *J. Adv. Ceram.*, 2019, **8**(1), 148–152.
25 T. Jin, X. Sang, R. R. Unocic, R. T. Kinch, X. Liu and J. Hu, *et al.*, *Adv. Mater.*, 2018, **30**(23), 1707512.
26 J. Zhou, J. Zhang, F. Zhang, B. Niu, L. Lei and W. Wang, *Ceram. Int.*, 2018, **44**(17), 22014–22018.
27 A. Sarkar, Q. Wang, A. Schiele, M. R. Chellali, S. S. Bhattacharya and D. Wang, *et al.*, *Adv. Mater.*, 2019, **31**(26), 1806236.
28 C. M. Rost, E. Sachet, T. Borman, A. Moballegh, E. C. Dickey and D. Hou, *et al.*, *Nat. Commun.*, 2015, **6**(1), 1–8.
29 A. Sarkar, B. Breitung and H. Hahn, *Scr. Mater.*, 2020, **187**, 43–48.
30 S. Akrami, P. Edalati, M. Fuji and K. Edalati, *Mater. Sci. Eng., R*, 2021, **146**, 100644.
31 Z. Rak, C. M. Rost, M. Lim, P. Sarker, C. Toher and S. Curtarolo, *et al.*, *J. Appl. Phys.*, 2016, **120**(9), 095105.
32 H. Li, H. Zhu, S. Zhang, N. Zhang, M. Du and Y. Chai, *Small Struct.*, 2020, **1**(2), 2000033.
33 Y. Yao, Z. Huang, P. Xie, S. D. Lacey, R. J. Jacob and H. Xie, *et al.*, *Science*, 2018, **359**(6383), 1489–1494.
34 R. Z. Zhang and M. J. Reece, *J. Mater. Chem. A*, 2019, **7**(39), 22148–22162.
35 D. Feng, Y. Dong, L. Zhang, X. Ge, W. Zhang, S. Dai and Z. A. Qiao, *Angew. Chem.*, 2020, **132**(44), 19671–19677.
36 M. Bondesgaard, N. L. N. Broge, A. Mamakhel, M. Bremholm and B. B. Iversen, *Adv. Funct. Mater.*, 2019, **29**(50), 1905933.
37 D. Redka, C. Gadelmeier, J. Winter, M. Spellauge, C. Eulenkamp and P. Calta, *et al.*, *Appl. Surf. Sci.*, 2021, **544**, 148839.
38 Y. S. Kim, H. J. Park, S. C. Mun, E. Jumaev, S. H. Hong and G. Song, *et al.*, *J. Alloys Compd.*, 2019, **797**, 834–841.
39 W. Zhao, F. Yang, Z. Liu, H. Chen, Z. Shao and X. Zhang, *et al.*, *Ceram. Int.*, 2021, **47**(20), 29379–29385.
40 Y. Xing, W. Dan, Y. Fan and X. A. J. Li, *Mater. Sci. Technol.*, 2022, **103**, 215–220.
41 J. Su, Z. Cao, Z. Jiang, G. Chen, Y. Zhu, L. Wang and G. Li, *Int. J. Appl. Ceram. Technol.*, 2022, **19**, 2004–2015.
42 C. Triolo, W. Xu, B. Petrovičovà, N. Pinna and S. Santangelo, *Adv. Funct. Mater.*, 2022, 2202892.
43 B. Petrovičovà, W. Xu, M. G. Musolino, F. Pantò, S. Patanè, N. Pinna, S. Santangelo and C. Triolo, *Appl. Sci.*, 2022, **12**, 5965.
44 X. Lu, C. Wang and Y. Wei, *Small*, 2009, **5**(21), 2349–2370.
45 M. J. Laudenslager, R. H. Scheffler and W. M. Sigmund, *Pure Appl. Chem.*, 2010, **82**(11), 2137–2156.
46 Z. Li and C. Wang, *One-dimensional nanostructures: electrospinning technique and unique nanofibers*, Springer Berlin Heidelberg, New York, Dordrecht, London, 2013, pp. 15–29.
47 Q. Liu, J. Zhu, L. Zhang and Y. Qiu, *Renewable Sustainable Energy Rev.*, 2018, **81**, 1825–1858.

48 S. Santangelo, *Appl. Sci.*, 2019, **9**(6), 1049.
49 Z. M. Stanojević, N. Romčević and B. Stojanović, *J. Eur. Ceram. Soc.*, 2007, **27**(2–3), 903–907.
50 J. Dąbrowa, M. Stygar, A. Mikuła, A. Knapik, K. Mroczka and W. Tejchman, *et al.*, *Mater. Lett.*, 2018, **216**, 32–36.
51 A. Mao, F. Quan, H. Z. Xiang, Z. G. Zhang, K. Kuramoto and A. L. Xia, *J. Mol. Struct.*, 2019, **1194**, 11–18.
52 D. Wang, S. Jiang, C. Duan, J. Mao, Y. Dong and K. Dong, *et al.*, *J. Alloys Compd.*, 2020, **844**, 156158.
53 H. Li, H. Zhu, S. Sun, J. Hao, Z. Zhu and F. Xu, *et al.*, *Chem. Commun.*, 2021, **57**(78), 10027–10030.
54 Z. Sun, Y. Zhao, C. Sun, Q. Ni, C. Wang and H. Jin, *Chem. Eng. Trans.*, 2022, **431**, 133448.
55 T. X. Nguyen, J. Patra, J. K. Chang and J. M. Ting, *J. Mater. Chem. A*, 2020, **8**(36), 18963–18973.
56 M. Stygar, J. Dąbrowa, M. Moździerz, M. Zajusz, W. Skubida and K. Mroczka, *et al.*, *J. Eur. Ceram. Soc.*, 2020, **40**(4), 1644–1650.
57 H. X. Guo, W. M. Wang, C. Y. He, B. H. Liu, D. M. Yu, G. Liu and X. H. Gao, *ACS Appl. Mater. Interfaces*, 2022, **14**(1), 1950–1960.
58 B. Talluri, M. L. Aparna, N. Sreenivasulu, S. S. Bhattacharya and T. Thomas, *J. Energy Storage*, 2021, **42**, 103004.
59 A. Sarkar, R. Kruk and H. Hahn, *Dalton Trans.*, 2021, **50**(6), 1973–1982.
60 S. K. Shaw, A. Gangwar, A. Sharma, S. K. Alla, S. Kavita, M. Vasundhara, S. S. Meena, P. Maiti and N. K. Prasad, *J. Alloys Compd.*, 2021, **878**, 160269.
61 A. Mao, H. Z. Xiang, Z. G. Zhang, K. Kuramoto, H. Zhang and Y. J. Jia, *Magn. Magn. Mater.*, 2020, **497**, 165884.
62 B. Musicó, Q. Wright, T. Z. Ward, A. Grutter, E. Arenholz, D. Gilbert, D. Mandrus and V. Keppens, *Phys. Rev. Mater.*, 2019, **3**(10), 104416.
63 G. Wang, J. Qin, Y. Feng, B. Feng, S. Yang, Z. Wang, Y. Zhao and J. Wei, *ACS Appl. Mater. Interfaces*, 2020, **12**(40), 45155–45164.
64 J. Cieslak, M. Reissner, K. Berent, J. Dabrowa, M. Stygar, M. Mozdzierz and M. Zajusz, *Acta Mater.*, 2021, **206**, 116600.
65 A. Sarkar, B. Eggert, R. Witte, J. Lill, L. Velasco, Q. Wang, J. Sonar, K. Ollefs, S. S. Bhattacharya, R. A. Brand, H. Wende, F. M. F. de Groot, O. Clemens, H. Hahn and R. Kruk, *Acta Mater.*, 2022, **226**, 117581.
66 J. Xiang, X. Shen, F. Song and M. Liu, *J. Solid State Chem.*, 2010, **183**(6), 1239–1244.
67 Z. Wang, X. Liu, M. Lv, P. Chai, Y. Liu, X. Zhou and J. Meng, *J. Phys. Chem. C*, 2008, **112**(39), 15171–15175.
68 A. Ponti, M. H. Raza, F. Pantò, A. M. Ferretti, C. Triolo and S. Patanè, *et al.*, *Langmuir*, 2020, **36**(5), 1305–1319.
69 Y. Li, H. Zhang, X. Zhang, L. Wei, Y. Zhang, G. Hai and Y. Sun, *J. Mater. Sci.: Mater. Electron.*, 2019, **30**(16), 15734–15743.
70 D. Hu, R. Wang, P. Du, G. Li, Y. Wang, D. Fan and X. Pan, *Ceram. Int.*, 2022, **48**, 6549–6555.
71 J. Dąbrowa, M. Stygar, A. Mikuła, A. Knapik, K. Mroczka and W. Tejchman, *et al.*, *Mater. Lett.*, 2018, **216**, 32–36.
72 H. Chen, N. Qiu, B. Wu, Z. Yang, S. Sun and Y. Wang, *RSC Adv.*, 2020, **10**(16), 9736–9744.
73 B. Liang, Y. Ai, Y. Wang, C. Liu, S. Ouyang and M. Liu, *Materials*, 2020, **13**(24), 5798.
74 T. X. Nguyen, J. Patra, J. K. Chang and J. M. Ting, *J. Mater. Chem. A*, 2020, **8**(36), 18963–18973.
75 Y. Zheng, X. Wu, X. Lan and R. Hu, *Processes*, 2022, **10**(1), 49.
76 B. Talluri, K. Yoo and J. Kim, *J. Environ. Chem. Eng.*, 2022, **10**(1), 106932.
77 A. L. Patterson, *Phys. Rev.*, 1939, **56**(10), 978.
78 R. Dronskowski, *Computational Chemistry of Solid State Materials*, Wiley-VCH Verlag GmbH & Co. KGaA, Weinheim, Germany, 2005, pp. 13–16.
79 R. D. Shannon, *Acta Crystallogr., Sect. A: Cryst. Phys., Diffr., Theor. Gen. Crystallogr.*, 1976, **32**, 751–767.
80 G. C. Allen, S. J. Harris, J. A. Jutson and J. M. Dyke, *Appl. Surf. Sci.*, 1989, **37**, 111–134.
81 E. Agostinelli, C. Battistoni, D. Fiorani, G. Mattogno and M. Nogues, *J. Phys. Chem. Solids*, 1989, **50**, 269–272.
82 G. P. Halada and C. R. J. Clayton, *Electrochem. Soc.*, 1991, **138**, 2921–2927.
83 J. F. Moulder, W. F. Stickle, P. E. Sobol and K. D. Bomben, *Handbook of X-ray Photoelectron Spectroscopy: A Reference Book of Standard Spectra for Identification and Interpretation of XPS Data*, Physical Electronics Division, PerkinElmer Corporation, Eden Prairie, Minnesota, USA, 1992, p. 55344.
84 G. Pagot, F. Bertasi, G. Nawn, E. Negro, G. Carraro, D. Barreca, C. Maccato, S. Polizzi and V. Di Noto, *Adv. Funct. Mater.*, 2015, **25**, 4032–4037.
85 G. Pagot, M. Bandiera, K. Vezzù, A. Migliori, R. Bertoncello, E. Negro, V. Morandi and V. Di Noto, *J. Mater. Chem. A*, 2020, **8**, 25727–25738.
86 S. Sepulveda-Guzman, B. Reeja-Jayan, E. de la Rosa, A. Torres-Castro, V. Gonzalez-Gonzalez and M. Jose-Yacaman, *Mater. Chem. Phys.*, 2009, **115**, 172–178.
87 M. Wang, L. Jiang, E. J. Kim and S. H. Hahn, *RSC Adv.*, 2015, **5**, 87496–87503.
88 V. M. Jiménez, A. Fernández, J. P. Espinós and A. R. González-Elipe, *J. Electron Spectrosc. Relat. Phenom.*, 1995, **71**, 61–71.
89 F. A. Bushira, P. Wang and Y. Jin, *Anal. Chem.*, 2022, **94**, 2958–2965.
90 J. Bao, X. Zhang, B. Fan, J. Zhang, M. Zhou, W. Yang, X. Hu, H. Wang, B. Pan and Y. Xie, *Angew. Chem., Int. Ed.*, 2015, **54**, 7399–7404.
91 J. H. Kim, Y. J. Jang, J. H. Kim, J. W. Jang, S. H. Choi and J. S. Lee, *Nanoscale*, 2015, **7**, 19144.
92 T. Dickinson, A. F. Povey and P. M. A. Sherwood, *J. Chem. Soc., Faraday Trans. 1*, 1976, **72**, 686–705.
93 V. Nefedov, D. Gati, B. Dzhurinskii, N. Sergushin and Y. V. Salyn, *Zh. Neorg. Khim.*, 1975, **20**, 2307–2314.
94 C. D. Wagner, D. A. Zatko and R. H. Raymond, *Anal. Chem.*, 1980, **52**, 1445–1451.
95 V. D'Ippolito, G. B. Andreozzi, D. Bersani and P. P. Lottici, *J. Raman Spectrosc.*, 2015, **46**(12), 1255–1264.
96 P. Choudhary and D. Varshney, *Mater. Res. Express*, 2017, **4**(7), 076110.

97 H. D. Lutz, B. Müller and H. J. Steiner, *J. Solid State Chem.*, 1991, **90**(1), 54–60.
98 B. Nandan, M. C. Bhatnagar and S. C. Kashyap, *J. Phys. Chem. Solids*, 2019, **129**, 298–306.
99 Z. Wang, R. T. Downs, V. Pischedda, R. Shetty, S. K. Saxena and C. S. Zha, *et al.*, *Phys. Rev. B: Condens. Matter Mater. Phys.*, 2003, **68**(9), 094101.
100 M. Foerster, M. Iliev, N. Dix, X. Martí, M. Barchuk, F. Sánchez and J. Fontcuberta, *Adv. Funct. Mater.*, 2012, **22**(20), 4344–4351.
101 R. Chen, W. Wang, X. Zhao, Y. Zhang, S. Wu and F. Li, *Chem. Eng. Trans.*, 2014, **242**, 226–233.
102 M. A. Laguna-Bercero, M. L. Sanjuán and R. I. Merino, *J. Condens. Matter Phys.*, 2007, **19**(18), 186217.
103 M. H. Abdellatif, A. A. Azab and M. Salerno, *Mater. Res. Bull.*, 2018, **97**, 260–264.
104 Z. Lazarević, Č. Jovalekić, A. Milutinović, D. Sekulić, V. N. Ivanovski and A. Rečnik, *et al.*, *J. Appl. Phys.*, 2013, **113**(18), 187221.
105 S. Supriya, S. Kumar and M. Kar, *J. Electron. Mater.*, 2019, **48**(6), 3612–3623.
106 L. Malavasi, P. Galinetto, M. C. Mozzati, C. B. Azzoni and G. Flor, *Phys. Chem. Chem. Phys.*, 2002, **4**(15), 3876–3880.
107 B. D. Hosterman, PhD thesis, University of Nevada, Las Vegas, 2011.
108 G. Datt, M. S. Bishwas, M. M. Raja and A. C. Abhyankar, *Nanoscale*, 2016, **8**(9), 5200–5213.
109 W. Wang, Z. Ding, X. Zhao, S. Wu, F. Li, M. Yue and J. P. Liu, *J. Appl. Phys.*, 2015, **117**(17), 17A328.
110 A. F. Wells, *Structural Inorganic Chemistry*, Clarendon Press, Oxford (UK), 2012.
111 A. R. West, *Solid State Chemistry and Its Applications*, Wiley, Chichester, West Sussex, UK, 2nd edn, student edn, 2014.
112 S. Chikazumi, Physics of Ferromagnetism, *The international series of monographs on physics*, Oxford University Press, Oxford (UK), 2nd edn, 1997.
113 O. F. Dippo and K. S. Vecchio, *Scr. Mater.*, 2021, **201**, 113974.
114 M. Fracchia, M. Manzoli, U. Anselmi-Tamburini and P. Ghigna, *Scr. Mater.*, 2020, **188**, 26–31.
115 T.-Y. Chen, S.-Y. Wang, C.-H. Kuo, S.-C. Huang, M.-H. Lin, C.-H. Li, H.-Y. T. Chen, C.-C. Wang, Y.-F. Liao, C.-C. Lin, Y.-M. Chang, J.-W. Yeh, S.-J. Lin, T.-Y. Chen and H.-Y. Chen, *J. Mater. Chem. A*, 2020, **8**(41), 21756–21770.
116 J. M. D. Coey, *Magnetism and Magnetic Materials*, Cambridge University Press, Cambridge (UK), 2013.
117 X. Batlle, M. García del Muro, J. Tejada, H. Pfeiffer, P. Görnert and E. Sinn, *J. Appl. Phys.*, 1993, **74**(5), 3333–3340.
118 B. D. Cullity and C. D. Graham, *Introduction to Magnetic Materials*, IEEE/Wiley, Hoboken, NJ, 2nd edn, 2009.
119 V. Tsurkan, H.-A. Krug von Nidda, J. Deisenhofer, P. Lunkenheimer and A. Loidl, *Phys. Rep.*, 2021, **926**, 1–86.
120 E. F. Kneller and F. E. Luborsky, *J. Appl. Phys.*, 1963, **34**(3), 656–658.
121 C. Zener, *Phys. Rev.*, 1954, **96**(5), 1335–1337.
122 J. Smit and H. P. J. Wijn, *Ferrites*, N.V. Philips' Gloeilampenfabrieken, Eindhoven (NL), 1959.
123 K. Tomiyasu, J. Fukunaga and H. Suzuki, *Phys. Rev. B: Condens. Matter Mater. Phys.*, 2004, **70**(21), 214434.
124 K. Tomiyasu and I. Kagomiya, *J. Phys. Soc. Jpn.*, 2004, **73**(9), 2539–2542.
125 S. Bordács, D. Varjas, I. Kézsmárki, G. Mihály, L. Baldassarre, A. Abouelsayed, C. A. Kuntscher, K. Ohgushi and Y. Tokura, *Phys. Rev. Lett.*, 2009, **103**(7), 077205.
126 R. Nepal, Q. Zhang, S. Dai, W. Tian, S. E. Nagler and R. Jin, *Phys. Rev. B: Condens. Matter Mater. Phys.*, 2018, **97**(2), 024410.
127 A. Mao, F. Quan, H.-Z. Xiang, Z.-G. Zhang, K. Kuramoto and A.-L. Xia, *J. Mol. Struct.*, 2019, **1194**, 11–18.